nature geoscience

Article

https://doi.org/10.1038/s41561-026-01962-x

Late Miocene Euphrates River drained into a partially desiccated eastern Mediterranean

Received: 31 March 2025

Accepted: 12 March 2026

Published online: 1 June 2026

Check for updates

Andrew S. Madof[1], Fabien J. Laugier[1], Sarah E. Baumgardner[2], Abdallah S. Zaki[3], Elise J. Laugier[4], Claudia Bertoni[5], Richard T. Walker[5], Carlos Rivero[2] & Simon C. Lang[6]

Although the Euphrates River—stretching ~3,000 km across Western Asia—has shaped the region's geology for millions of years, the timing of its origin and the evolution of its course remain enigmatic. So far, two contrasting hypotheses have been proposed to explain the fluvial system's Late Neogene path: termination in Anatolia at a palaeo-lake or the Mediterranean, or a southeastward continuation to Arabia. Here we use seismic-reflection and topographic data to show that two previously identified sedimentary accumulations—deposited during the terminal phase of the Late Miocene Messinian salinity crisis—resulted from dual riverine systems that drained into a partially desiccated eastern Mediterranean before avulsing toward the Persian Gulf and converging to form the modern Euphrates River. From probabilistic sediment-budget modelling, we show that although the latest Messinian drainage basins were an order of magnitude smaller than their present-day extents, the total palaeo-discharge exceeded that of the modern Tigris, Euphrates and Nile rivers combined, indicating intense palaeo-precipitation and high palaeo-relief. These results suggest that plate-margin deformation both controlled the fluvial avulsions that diverted the Euphrates River from the Anatolian–Eurasian Plate to the Arabian Plate, and established the conditions necessary for the development of the alluvial Fertile Crescent.

From the early Pleistocene traces of human ancestors two million years ago (Ma)[1] to the rise of the world's oldest-known cities ~3,500 BCE (Before the Common Era)[2], the Euphrates River has long been intertwined with human history. According to ancient Mesopotamian creation myths, the Euphrates River was formed by Enki, God of wisdom and water, during the birth of the world[3]. Yet, current geologic–geomorphic evidence suggests that the fluvial system emerged as recently as ~10 Ma (ref. 4), during the Tortonian age of the Late Miocene epoch. Some researchers suggest that the early Euphrates River ended at endorheic palaeo-lakes in Anatolia—or possibly the Mediterranean—while others argue it followed a southeastward course[5], terminating in the arid landscapes of Arabia. In either case, these hypotheses remain divergent, leaving the evolution of the early Euphrates River elusive.

In this Article we establish a direct link between two previously identified fluvio-lacustrine accumulations—the Handere[6] and Nahr Menashe[7]—and the ancestral Euphrates River, which we hypothesize began as dual riverine systems. We posit that these fluvial networks initially emptied into shallow upland basins before discharging into a partially desiccated eastern Mediterranean—a transformation we attribute

[1]International Exploration and Production, Chevron, Houston, TX, USA. [2]Technical Center, Chevron, Houston, TX, USA. [3]Department of Earth and Planetary Sciences, Jackson School of Geosciences, The University of Texas at Austin, Austin, TX, USA. [4]Department of Environment and Society, Utah State University, Logan, UT, USA. [5]Department of Earth Sciences, University of Oxford, Oxford, UK. [6]School of Earth Sciences, The University of Western Australia, Perth, Western Australia, Australia. e-mail: andrew.madof@chevron.com

to the Late Miocene Messinian salinity crisis (MSC; 5.97–5.33 Ma)[8,9]. The Handere and Nahr Menashe were emplaced during this event, when the MSC drove the accumulation of >1 × 10^6 km^3 of evaporites and associated sediments[10] and triggered large-scale, regional fluvial incision[11]. To trace the origins of the Handere and Nahr Menashe—and their connection to Euphrates River drainage—we have conducted detailed geologic–geomorphic mapping and identified two potential fluvial pathways that may have sourced them. From fault reconstructions, we constrained the ancient positions of these systems, which we interpret as the palaeo-equivalents of the modern Karasu and Murat rivers, the two main tributaries of the Euphrates River. Using probabilistic sediment-budget modelling, we have quantified the catchment surface areas, sediment–water discharge rates and sediment provenances of these ancient rivers, which we term the Palaeo-Karasu and Palaeo-Murat. Our findings refine the palaeogeography of the partially desiccated eastern Mediterranean during the MSC, revealing a previously unrecognized proximity between the ancestral Euphrates and Nile rivers. Finally, we propose a tectonic mechanism to explain the avulsions that reconfigured the Palaeo-Karasu and Palaeo-Murat rivers, thereby leading to the formation of the present-day Euphrates River and alluvial Fertile Crescent.

Miocene–Pliocene pathways

Although the Handere and Nahr Menashe are well studied in the offshore eastern Mediterranean, their onshore equivalents remain poorly understood. To address this issue, we used published maps of the Handere (offshore Türkiye)[12] and re-mapped the entirety of the Nahr Menashe (offshore Syria, Lebanon, Israel, Cyprus and Egypt) on 192 two-dimensional (2D) seismic-reflection lines and five three-dimensional (3D) seismic-reflection volumes (Methods and Extended Data Fig. 1). By integrating the geologic map of Türkiye[13] with Shuttle Radar Topography Mission (SRTM) imagery, we traced subsurface extensions onshore, identifying potential palaeo-pathways that may have sourced these fluvial accumulations. Where mapped pathways (linear or meandering, topographic troughs associated with active or abandoned channels and overlying Late Miocene to Early Pliocene riverine deposits) intersected faults[14], we used offset lengths[15] and long-term slip rates to constrain ages and chronologies. Despite the challenges of mapping palaeo-channels in tectonically active, mountainous terrains, our high-quality data and the region's exceptionally well-constrained geology validated our approach. Similar topographic-based methods have been used successfully to identify Miocene channels in Libya[16] and to reconstruct ages using fluvial offsets in Iran[17].

Our analyses yielded four key observations linking modern riverine systems to ancient fluvial deposits: (1) the upper Karasu and Murat rivers align azimuthally with the Handere and Nahr Menashe, respectively; (2) Late Miocene to Early Pliocene fluvio-lacustrine accumulations are present downstream of major bends in the lower Karasu and Murat rivers; (3) continuous modern riverine paths connect the upper Karasu and Murat rivers to the Handere and Nahr Menashe; and (4) the thickest deposits of the Handere and Nahr Menashe lie directly beneath current fluvial outflows into the eastern Mediterranean. Taken together, we interpret these observations to suggest that the present-day landscape reflects inheritance from Late Miocene topography. Consequently, we conclude that (1) similar large-scale structural trends controlled the alignment of the Karasu River, Murat River, Handere and Nahr Menashe; (2) palaeo-riverine flow was initially directed southwest before shifting southeast; (3) modern fluvial pathways preserve relict features of ancient systems; and (4) long-term riverine accumulation has persisted at the Mediterranean coastline.

Supported by high-resolution mapping, our findings show that during the Late Miocene, the Palaeo-Karasu and Palaeo-Murat rivers were approximately parallel, northeast–southwest-oriented systems that extended from their current headwaters to what is now offshore Türkiye and Syria (Fig. 1a). The Palaeo-Karasu River (length >1,370 km; sinuosity >1.75) encompassed segments of the Karasu River, Çaltı Suyu Stream, Karaboğaz Stream, Kangal Stream, Mancınık Creek, Zamantı River, Sehyan River and several unnamed creeks. In contrast, the Palaeo-Murat River (length >1,990 km; sinuosity <1.65) included portions of the Murat River, Sultansuyu Creek, Sürgü Stream, Göksu Stream, Aksu Stream, Karasu Stream, Orontes River, Nahr al-Kabir al-Shamali and other unnamed creeks.

Avulsion-fault chronology

At upstream positions, we infer that Early Pliocene avulsion redirected the Palaeo-Murat River towards the Persian Gulf, and in the Late Pliocene, the Palaeo-Karasu River was merged with it (Fig. 1b). Avulsion nodes, which we identified at deviations in trends of our mapped palaeo-pathways relative to modern fluvial channels, coincide with three key geomorphic features: local topographic lows, surface-gradient reversals and the confluence of tributaries with their mainstems. Together, these criteria suggest that avulsion nodes for the Palaeo-Murat River (Fig. 1c) occurred at the confluence of the modern Aksu Stream (tributary) with the Göksu Stream (mainstem), and for the Palaeo-Karasu River (Fig. 1d) they were situated at the confluence of the Çaltı Suyu Stream (tributary) with the Karasu River (mainstem). The final major avulsion, in the Pleistocene, occurred at the confluence of the Sultansuyu Creek (tributary) with the Euphrates River (mainstem) (Fig. 1e). Although our interpretation of avulsion timing and location is necessarily tentative without palaeo-current data, it closely parallels that of ref. 5, which identified major deflections in the Late Neogene Euphrates River using independent methodologies.

In conjunction with avulsion histories, we used fault offset lengths and long-term slip rates to invert for geologic age, establishing a chronological framework for the Palaeo-Karasu, Palaeo-Murat and Euphrates rivers. Although this method introduces uncertainty due to assumptions of constant fault slip rates and stable riverine courses, it currently remains the only practical approach for estimating geologic age in the absence of direct dating methods. Consequently, we find that in the Erzincan Basin, the Palaeo-Karasu River crossed the North Anatolian Fault (NAF) at ~8.6 Ma, following fault activation at ~12 Ma (ref. 18; Fig. 1f). To the southwest in the northern Malatya Basin, the system traversed the Ovacık Fault at ~2.8 Ma, several million years after its activation at ~7–6 Ma (ref. 19; Fig. 1g). Further southeast, in the eastern Elazığ Basin, the Palaeo-Murat River intersected the East Anatolian Fault (EAF) at ~4.3 Ma, coinciding with or preceding its reactivation (ref. 20; Fig. 1h). In the southern Malatya Basin, the Euphrates River crossed the westward-younging EAF at ~3.6 Ma (Fig. 1i); by ~1.6 Ma, the Euphrates River had again traversed the EAF in the western Elazığ Basin to the northeast (Fig. 1j).

To interpret the mechanisms of avulsion, we extracted topographic profiles along the proposed paths of the Palaeo-Karasu, Palaeo-Murat and Euphrates rivers (Methods and Fig. 2a,b). Based on the geologic evolution of the area and our interpreted avulsion nodes—located at the bases of elevated terranes—we infer that the ancient riverine systems were diverted due to a combination of long-wavelength uplift[21] and short-wavelength faulting[18,20,22–26]. These processes—which exerted a first-order control on the drainage evolution and sediment routing across eastern Anatolia—were probably driven by distributed lithospheric compression[27], asthenospheric–lithospheric slab peel-back[28], and/or elevated asthenospheric temperatures[21]. Consequently, tilting of eastern Anatolia since the Late Oligocene steepened the regional gradient, which, along with Late Miocene faulting, partitioned the landscape and promoted flow capture. Stratigraphic evidence from the Kangal[29] and Malatya basins[30] supports our interpretation, as Late Miocene to Early Pliocene coal at relatively high (modern) elevations points to topographic inversion of once low-lying, poorly drained areas. Despite the Late Pliocene to recent post-depositional deformation, pre-uplift

https://doi.org/10.1038/s41561-026-01962-x

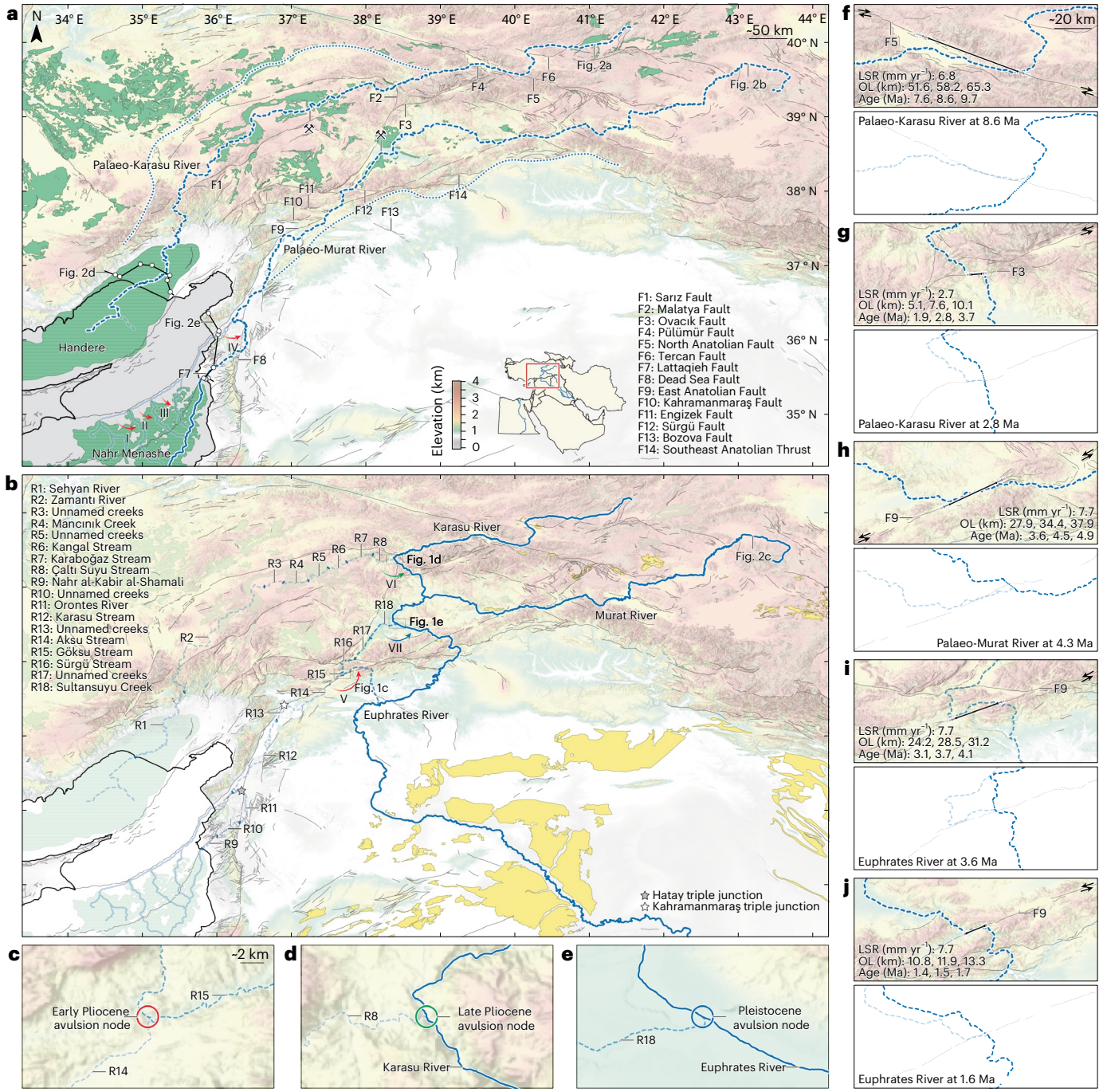

Fig. 1 | Paths of the ancestral and modern Euphrates River in Western Asia. **a**, The Late Miocene Euphrates River consisted of two fluvial systems—the Palaeo-Karasu and Palaeo-Murat rivers (dashed blue lines—proposed pathways)—which flowed into the eastern Mediterranean and deposited the Handere[6] and Nahr Menashe[7]. Mixed-lithologic accumulations in present-day positions: surface (Late Miocene–Early Pliocene, solid green polygons)[13]; subsurface (Late Miocene, hatched green polygons)[7,12]. Coal mines are marked by hammer and pick symbols. The proposed avulsion order is from older (I) to younger (IV). Surface faults[14] are noted. Blue dotted lines delineate the zone of lateral uncertainty for reconstructed pathways. **b**, The Early Pliocene Palaeo-Murat River avulsed eastward, being joined by the Palaeo-Karasu River in the Late Pliocene. The system avulsed again in the Pleistocene, forming the modern Euphrates River. Modern fluvial systems reoccupy ancestral pathways. Siliciclastic deposits are shown at the surface (undifferentiated Pliocene, yellow polygons)[60]. Triple junctions are indicated by stars. **c**–**e**, Avulsion nodes in the Early Pliocene (**c**), Late Pliocene (**d**) and Pleistocene (**e**). **f**–**j**, Long-term slip rates (LSRs)[18,20,22–26] and offset lengths (OLs) of strike–slip faults were used to calculate segment ages, which are shown reconstructed at their means: Palaeo-Karasu River at 8.6 Ma (**f**) and 2.8 Ma (**g**); Palaeo-Murat River at 4.3 Ma (**h**); and Euphrates River at 3.6 Ma (**i**) and 1.6 Ma (**j**). Basemaps created in ArcGIS Pro 3.0.2 with data from the United States Geological Survey (USGS) EarthExplorer (https://www.usgs.gov/tools/earthexplorer).

paths of the Palaeo-Karasu and Palaeo-Murat rivers probably resembled that of the current Euphrates River (ref. 31; Fig. 2c). Downstream at the Mediterranean coastline, the reconstructed riverine systems overlie the thickest accumulations of the Handere (Fig. 2d) and Nahr Menashe (Fig. 2e), providing evidence for sustained fluvial activity. Although long-term uplift and faulting are interpreted as the primary controls on riverine diversion, short-term palaeo-seismicity and/or palaeo-earthquakes cannot be ruled out, as avulsion nodes are situated

https://doi.org/10.1038/s41561-026-01962-x

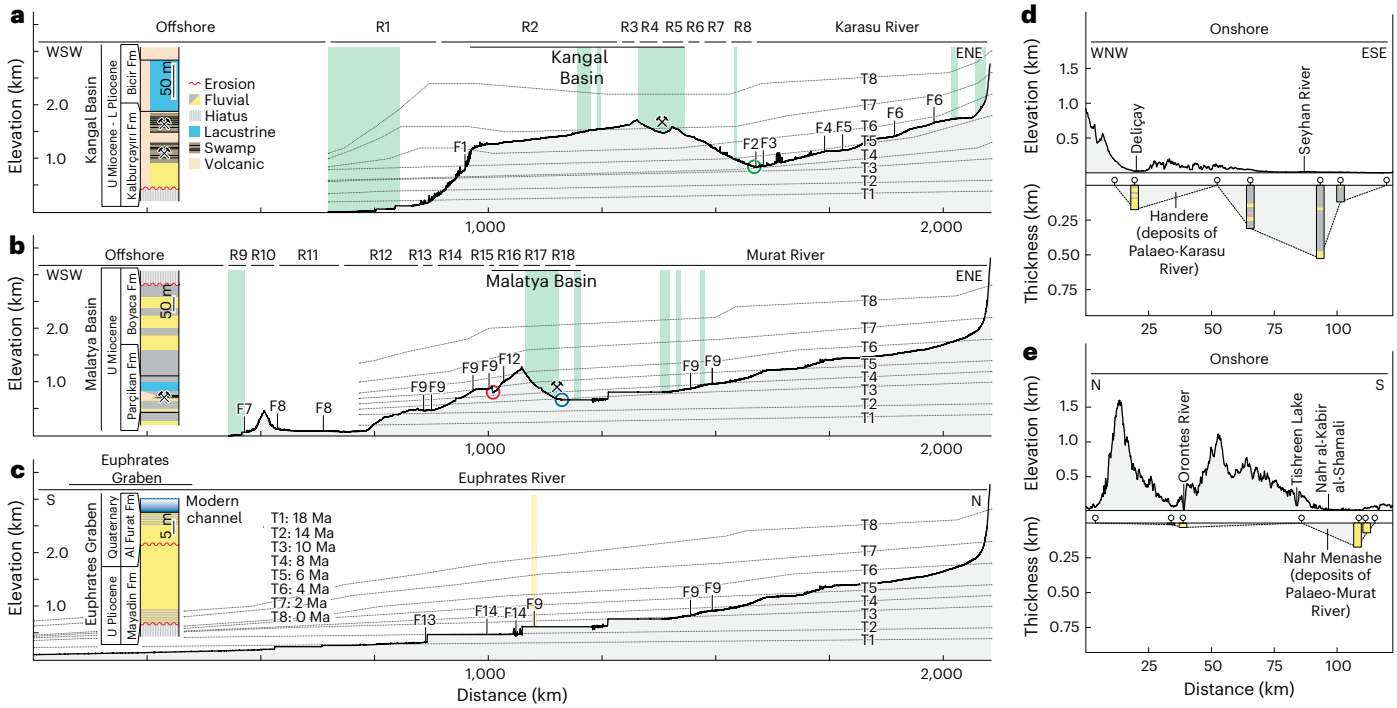

Fig. 2 | Topographic profiles and subsurface sediment thicknesses. a–**c**, Profiles along the Palaeo-Karasu (**a**), Palaeo-Murat (**b**) and modern Euphrates (**c**) rivers, showing the present-day distribution of Late Miocene to Early Pliocene deposits (green highlighted areas), undifferentiated Pliocene-aged accumulations (yellow highlighted area) and fault traces at the surface. The locations of avulsion nodes in Early Pliocene (red ring), Late Pliocene (green ring) and Pleistocene (blue ring) are interpreted to have been caused by deformation associated with uplift and faulting. Long-wavelength cumulative uplift (grey dotted lines) over the last 18 Myr is from ref. 21. See Fig. 1a,b for location of profiles and legends. Coal mines are marked by hammer and pick symbols. Stratigraphic columns are from refs. 29 (**a**), 30 (**b**) and 31 (**c**). **d**,**e**, Surface profiles at the coast, displayed over Late Miocene deposits at depth[61–68]. Spatial correspondences of current fluvial systems to the thickest accumulations of the Handere (**d**) and Nahr Menashe (**e**) are interpreted to represent topographic inheritance from the Late Miocene.

on or near plate boundaries and faults, including the epicentre of the 7.8-magnitude 2023 Kahramanmaraş (Türkiye) earthquake[32], located ~90 km south-southwest of the Palaeo-Murat River's avulsion site.

Sediment-budget modelling

Using our mapped palaeo-pathways, we modelled the Late Miocene sediment budget of the Palaeo-Karasu and Palaeo-Murat basins during the terminal phase of the MSC (~5.45–5.33 Ma) using a probabilistic approach to the empirical BQART model (Methods)[33]. Although we recognize the existence of alternative approaches—including source-to-sink models[34]—we selected BQART to estimate sediment discharge based on basin parameters (such as surface area, water discharge, relief, temperature, lithology and trapping efficiency). Given known sediment volumes, durations and discharges for the Handere (8,313 km^3, this study; 120 kyr from biostratigraphy and geochronology, ref. 6; 139.2 MT yr^{-1}, this study) and the Nahr Menashe (3,372 km^3, this study; 120 kyr, consistent with ref. 6; 56.2 MT yr^{-1}, this study), we inverted the BQART model to estimate basin areas (Extended Data Table 1a,b). Model runs for the Palaeo-Karasu (Extended Data Fig. 2a–f) and Palaeo-Murat (Extended Data Fig. 3a–f) rivers returned median (P50) basin areas of ~2.5×10^5 km^2 and ~9.9×10^4 km^2, respectively (Fig. 3a). As a validation step, we compared modelled basin areas with those derived from an empirical relationship linking river length and catchment shape (modified Hack's law)[35], and the results suggest that while the Palaeo-Karasu River was relatively immature (or rejuvenated), the Palaeo-Murat River was more established. Reconstructed catchment geometries, based on P50 basin areas, plate boundaries, position of the Black Sea, and Late Miocene to Early Pliocene onshore deposits, indicate that the Palaeo-Karasu Basin extended westward into Anatolia, whereas the Palaeo-Murat Basin remained constrained by the Arabian Plate margin (Fig. 3b). Larger catchments are unlikely, as they would have required evidence of systems far beyond the geologic–geomorphic boundaries identified above.

To test our hypotheses regarding ancient catchments, we used Türkiye's geologic map alongside existing lithologic data. A previous study focusing on the northern Handere[6], which employed clast counts of conglomerates from six outcrop sites, revealed that >75% of the deposit consisted of carbonate, volcanic and undifferentiated sedimentary rocks, with the remainder comprising metamorphic and igneous rocks (ophiolitic and non-ophiolitic). When compared to lithologies along our reconstructed Palaeo-Karasu River path, the rock types are remarkably similar (Fig. 3c). However, the Palaeo-Karasu Basin includes two lithologies absent in northern Handere samples: evaporitic rocks, likely dissolved and thus not deposited; and volcanic-sedimentary rocks, which constitute a mere 3% of the basin's surface area. Plotting point counts of the six shared rock types from the Handere against the surface area percentage of the exposed lithology of the Palaeo-Karasu Basin yields an r^2 value of 0.35, indicating a weak correlation. However, excluding accumulations located farther from the palaeo-channel—undifferentiated sedimentary rocks to the west—the r^2 value increases to 0.93, suggesting a strong relationship. This finding implies that the P50 basin area indicated by our model may be an overestimation. Regarding the Nahr Menashe (Fig. 3d), the International Ocean Discovery Program (IODP)[36] approved sampling at eight sites; however, the program's termination precluded drilling, leaving the deposit unsampled. Yet, based on catchment lithology and the anomalously high seismic velocities of the deposit (2,925 m s^{-1})[7], the Nahr Menashe may contain elevated proportions of volcanic, carbonate, evaporitic and/or metamorphic rocks.

Expanding on these findings, we compared the reconstructed hydrology of the Palaeo-Karasu and Palaeo-Murat rivers with that of modern fluvial systems. Although the reconstructed basin areas were

https://doi.org/10.1038/s41561-026-01962-x

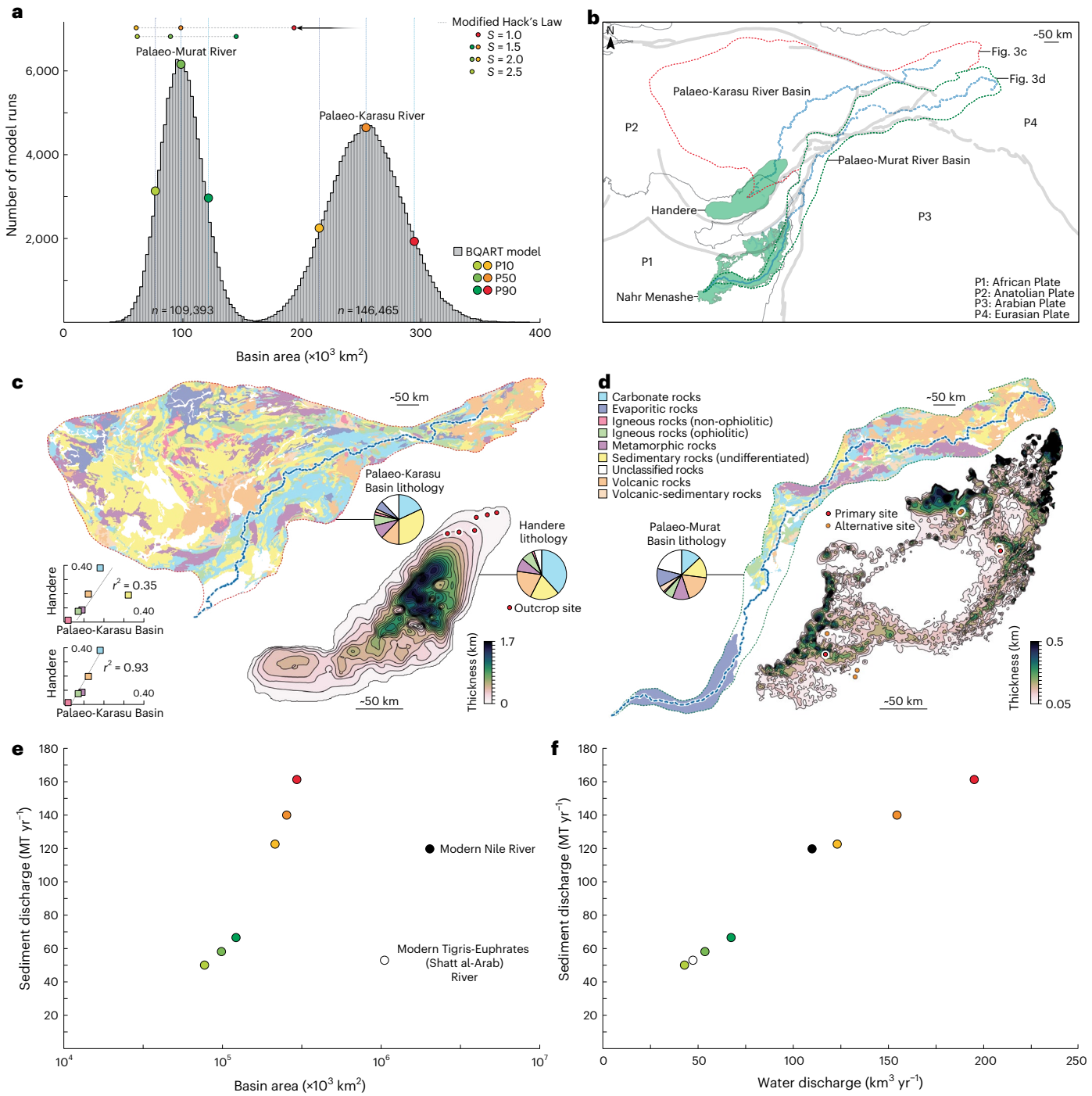

Fig. 3 | Reconstructed basin area, provenance, and sediment–water discharge. **a**, Results of the probabilistic sediment-budget model for basin areas of the Palaeo-Karasu and Palaeo-Murat rivers. *S* denotes catchment shape (1 = circular and 2.5 = elongate; Methods). **b**, P50 maps of basin areas, constrained by the locations of plate margins and Late Miocene to Early Pliocene-aged deposits. **c**,**d**, Lithology of modern landscape[13] constrained by P50 basin areas for the Palaeo-Karasu (**c**) and Palaeo-Murat (**d**) rivers, and isopach maps for the Handere (**c**) and Nahr Menashe (**d**). The Handere lithology was sampled from clast counting at six outcrop sites[6]. Nahr Menashe is currently unsampled, although eight sites were approved to be drilled during IODP Expedition 857C[36], prior to termination of the IODP program. Cross plots in **c** show percentages of Handere lithology versus the lithology of the Palaeo-Karasu Basin (top, six shared lithologies; bottom, six shared lithologies with sedimentary rocks removed). **e**, Sediment discharge versus basin area for the Palaeo-Karasu, Palaeo-Murat, modern Nile[69] and modern Tigris–Euphrates[69] rivers. **f**, Sediment discharge versus water discharge for the riverine systems in **e**. Elevated values for the Palaeo-Karasu and Palaeo-Murat rivers are attributed primarily to Late Miocene palaeo-precipitation and palaeo-relief. Basemap in **b** created in ArcGIS Pro 3.0.2. Panel **c** reproduced with permission from ref. 12, Elsevier.

roughly an order of magnitude smaller than the present-day Tigris–Euphrates and Nile river catchments (Fig. 3e), sediment discharge remained strikingly similar. To place these values in a palaeo-hydrologic context, we also compared them with the Rhône River during the MSC[37]: the Palaeo-Karasu River carried ~2.5 times the sediment discharge, whereas the Palaeo-Murat River was nearly identical. With respect to water discharge, the reconstructed P10, P50 and P90 values of the Palaeo-Karasu River exceeded those of the modern Nile River, while

https://doi.org/10.1038/s41561-026-01962-x

Fig. 4 | Reconstructed eastern Mediterranean during the terminal Messinian salinity crisis. View to the north-northeast at ~200-km altitude showing partial basin-wide desiccation at ~5.35 Ma. The Handere was deposited north of Cyprus, whereas the Nahr Menashe and Abu Madi accumulated south of the Eratosthenes Seamount. Note the proximity of the Palaeo-Euphrates and Palaeo-Nile rivers. The palaeogeographic model integrates published data and this study to constrain onshore–offshore palaeo-elevations[21,41] and delineate facies[6,7,12,13,42]. Inset map created in ArcGIS Pro 3.0.2 with data from Google. Credit: reconstruction, Lina Jakaitė and Andrew S. Madof.

for the Palaeo-Murat River, only the P10 fell below the present-day Tigris–Euphrates River (Fig. 3f). This paradoxical result—showing that during one of Earth's driest intervals (MSC), the Palaeo-Karasu and Palaeo-Murat rivers sustained higher water discharge than the largest rivers of modern Northern Africa and Western Asia, respectively—suggests that the palaeo-precipitation[38] and/or palaeo-temperature varied substantially, even at the scale of individual catchments. While Late Neogene climate models generally predict low-intensity rainfall across Western Asia[39,40], our sediment-budget models indicate higher average palaeo-precipitation, episodic high-intensity rainfall and/or localized hydrologic amplification. Combined with catchment size, these factors provide a more viable mechanism for the widespread occurrence of well-developed, Late Miocene to Early Pliocene lacustrine and mire (coal) deposits throughout eastern and central Anatolia.

Palaeogeographic reconstruction

To complement our upstream catchment analysis, we reconstructed the downstream palaeogeography of the Palaeo-Karasu and Palaeo-Murat rivers prior to avulsion (Fig. 4 and Methods). Our reconstruction (Extended Data Table 2), informed by the results of this study, fluvio-lacustrine depositional analogues and published interpretations of palaeo-elevations[21,41] and facies[6,7,12,13,42], constrained the eastern Mediterranean at ~5.35 Ma during the terminal stage of the MSC[43]. At that time, the Palaeo-Murat River had deposited much of the Nahr Menashe into a partially desiccated, westward-tilting Levant Basin east and south of the Eratosthenes Seamount. Seismic geometry indicates that this river was a single, large fluvial system that terminated in a palaeo-lake, which deepened westward towards the Herodotus Basin[7]. At its southern boundary, the Palaeo-Murat—that is, the ancestral Euphrates River—was separated by less than ~25 km from the northern limit of the Palaeo-Nile River, probably the shortest distance to separate these two rivers in Earth's history. North of Cyprus, the Palaeo-Karasu River deposited the Handere within the actively subsiding and subaerially exposed Adana and Cilicia basins; seismic and outcrop geometries suggest that this system may have also been supplemented by secondary coastal rivers[12,44]. In juxtaposition to the depositional sink of the Palaeo-Karasu and Palaeo-Murat rivers—the now submerged eastern Mediterranean drylands—their Anatolian–Eurasian source was marked by humid wetlands.

Euphrates River evolutionary model

We present, here, a conceptual model for the evolution of the Palaeo-Murat and Palaeo-Karasu rivers (Fig. 5a) that explains the emergence of the modern Euphrates River. Our fault chronology, coupled with volcanic ages from the Malatya[45] and Kangal[46] basins, suggests that the Palaeo-Murat River initiated on the Anatolian–Eurasian Plates after ~16.55 Ma, whereas the Palaeo-Karasu River developed between ~8.6 and ~5.9 Ma. Stratigraphic evidence indicates that by the Tortonian, both rivers drained into poorly connected, organic-rich lakes south of the NAF (Fig. 5b). By the late Messinian, shoaling across the Betic and Rifian corridors in the western Mediterranean (Strait of Gibraltar)[47,48] triggered a dramatic, basin-wide evaporitic drawdown, lowering the eastern Mediterranean's base level by ~1.7–2.1 km (ref. 49). Although some studies challenge the magnitude of this reduction[50,51], our sediment-budget model indicates that at least ~0.8 km of base-level lowering was necessary to fit the modelled catchment areas. Associated

https://doi.org/10.1038/s41561-026-01962-x

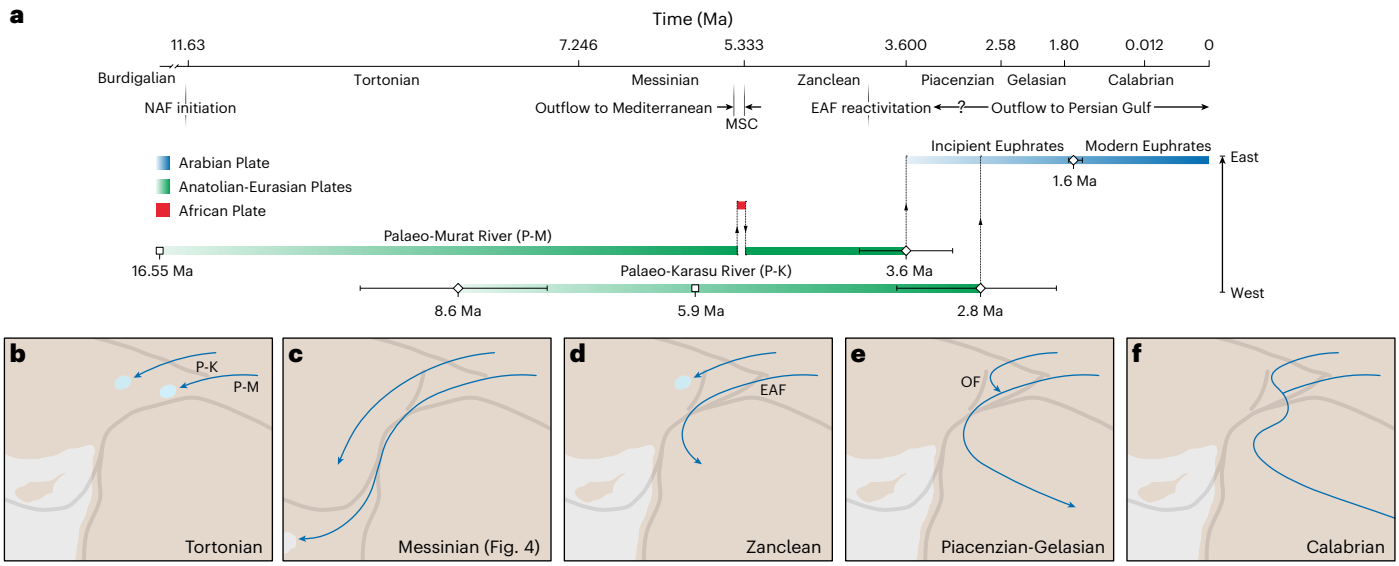

Fig. 5 | Temporal evolution and formation model for the Euphrates River. **a**, The Late Miocene ancestral Euphrates River initiated on the Anatolian–Eurasian Plates as the Palaeo-Murat and Palaeo-Karasu rivers. At ~3.6 Ma, the Palaeo-Murat River avulsed to the Arabian Plate, with the Palaeo-Karasu River avulsing to join it by ~2.8 Ma. The merged system became the modern Euphrates River by ~1.6 Ma. Before that, the incipient Euphrates River occupied a position to the south. Age control is from volcanics that underlie and are interbedded with fluvial strata (white squares)[45,46] and from fault reconstructions (white diamonds denote means, with bars indicating temporal uncertainty ranges; see Fig. 1f–j and Methods). EAF, East Anatolian Fault (~4-Ma reactivation); MSC, Messinian salinity crisis; NAF, North Anatolian Fault (~12-Ma initiation). **b**–**f**, Graphical representations of the chronology in **a**. By the Tortonian (**b**), the Palaeo-Karasu and Palaeo-Murat rivers terminated at lakes; during the Messinian (**c**) the systems flowed into the eastern Mediterranean during the kilometre-scale drawdown associated with the terminal phase of the MSC. In the Zanclean (**d**), the Palaeo-Murat River avulsed to the Arabian Plate due to reactivation of the EAF, while in the Piacenzian (**e**), the Palaeo-Karasu River avulsed due to decreased slip along the Ovacık Fault (OF). The final diversion of the Euphrates River in the Calabrian (**f**) is related to either local subsidence or landscape readjustment.

MSC-driven riverine incision—amplified by Anatolian tilting and fault reactivation—forced fluvial systems to readjust to a markedly lower base level, which intensified sediment delivery along faults and into the eastern Mediterranean (Fig. 5c). Given that this process probably triggered the sudden breaching of perched lakes in the Anatolian uplands, we hypothesize that the Handere and Nahr Menashe may have formed via lake-breach mega-floods, a mechanism analogous to surface dynamics on Earth[52] and early Mars[53]. However, further modelling is required to test this hypothesis, particularly to account for long run-out distances, which are conceptually difficult to reconcile without invoking catastrophic mechanisms. A similar process is envisaged for the Eosahabi fan—one of the largest known Messinian-aged fluvial deposits in the Mediterranean—offshore Sirt Basin (Libya)[54], which was probably fed by rapidly incising onshore drainage networks that responded to late Messinian base-level fall[55].

Chronologic constraints from the Handere and Nahr Menashe indicate that fluvial systems were active in now offshore areas between ~5.45 and 5.33 Ma, with the Palaeo-Karasu River maintaining flow across the Anatolian–Eurasian Plates throughout this 120-kyr interval. For the Palaeo-Murat River, drainage persisted on the Anatolian–Eurasian Plates from ~5.45 to 5.43 Ma (one depositional cycle; ~22 kyr)[56,57], after which flow was redirected onto the African Plate from ~5.43 to 5.33 Ma (four and half depositional cycles; ~98 kyr). Along with uplift and faulting, as well as the re-filling of the Mediterranean during the Zanclean mega-flood[58], the Miocene–Pliocene boundary (5.33 Ma) was marked by the abrupt landward retreat of fluvial systems and the cessation of accumulation to now offshore areas. In the Kangal Basin, the Palaeo-Karasu River deposited lacustrine sediments, suggesting that deformation produced intra-plate sub-basins actively infilled by terminal lakes. In the Murat Basin, erosional truncation of Late Miocene-aged accumulations records riverine avulsion, with drainage deflected away from areas of uplift[59] and towards the Arabian Plate.

At ~3.6 Ma (Fig. 5d), reactivation of the EAF diverted the Palaeo-Murat River southeastward, establishing its course on the Arabian Plate and marking the onset of the incipient Euphrates River. By ~2.8 Ma (Fig. 5e), decreased activity along the Ovacık Fault[26] promoted avulsion of the Palaeo-Karasu River towards the southeast, where it merged with the incipient Euphrates River. Although we interpret the mechanisms of diversion for the Palaeo-Murat and Palaeo-Karasu rivers to have been fundamentally tectonic in origin, the final northward-propagating avulsion of the incipient Euphrates River remains less clear. We hypothesize that this avulsion may have been driven by local subsidence or landscape readjustment, as the avulsion node currently sits in a local topographic low. Regardless of mechanism, we interpret the modern Euphrates River to have begun on the Arabian Plate at ~1.6 Ma (Fig. 5f).

Conclusion

We propose a framework to elucidate the enigmatic origins of the modern Euphrates River. Our findings indicate that this key historical river began as two distinct fluvial systems that briefly flowed into a marine basin, traversed four tectonic plates, converged, and ultimately emptied into a gulf. Regional deformation appears to have been an active and important process that exerted profound control over fluvial dynamics. We anticipate these conclusions will provide a more comprehensive understanding of the spatio-temporal evolution of Western Asia's riverine systems and offer deeper context for the terrestrial processes that laid the foundation for one of the world's oldest-known civilizations.

Online content

Any methods, additional references, Nature Portfolio reporting summaries, source data, extended data, supplementary information, acknowledgements, peer review information; details of author contributions and competing interests; and statements of data and code availability are available at https://doi.org/10.1038/s41561-026-01962-x.

References

1. Ozherelyev, D. V. et al. Early Palaeolithic evidence from the Euphrates River basin, eastern Turkey. *Quat. Int.* **509**, 73–86 (2019).
2. Morozova, G. S. A review of Holocene avulsions of the Tigris and Euphrates rivers and possible effects on the evolution of civilizations in Lower Mesopotamia. *Geoarchaelogy* **20**, 401–423 (2005).
3. Black, J., Cunningham, G., Robson, E. & Zólyomi, G. *The Literature of Ancient Sumer* (Oxford Univ. Press, 2004).
4. Demir, T. et al. Late Cenozoic regional uplift and localised crustal deformation within the northern Arabian Platform in southeast Turkey: investigation of the Euphrates terrace staircase using multidisciplinary techniques. *Geomorphology* **165–166**, 7–24 (2012).
5. Demir, T. et al. Location of the River Euphrates in the Late Miocene; dating of the terrace gravel at Shireen, Syria. *eEarth* **2**, 27–34 (2007).
6. Radeff, G. et al. Sedimentary evidence for late Messinian uplift of the SE margin of the Central Anatolian Plateau: Adana Basin, southern Turkey. *Basin Res.* **29**, 488–514 (2017).
7. Madof, A. S., Bertoni, C. & Lofi, L. Discovery of vast fluvial deposits provides evidence for drawdown during the late Miocene Messinian salinity crisis. *Geology* **47**, 171–174 (2019).
8. Hsü, K. J., Ryan, W. B. F. & Cita, M. B. Late Miocene desiccation of the Mediterranean. *Nature* **242**, 240–244 (1973).
9. Manzi, V. et al. Age refinement of the Messinian salinity crisis onset in the Mediterranean. *Terra Nova* **25**, 315–322 (2013).
10. Haq, B., Gorini, C., Baur, J., Moneron, J. & Rubino, J.-L. Deep Mediterranean's Messinian evaporite giant: how much salt? *Glob. Planet. Change* **184**, 103052 (2020).
11. Ryan, W. B. F. & Cita, M. B. The nature and distribution of Messinian erosional surfaces—indicators of a several-kilometre-deep Mediterranean in the Miocene. *Mar. Geol.* **27**, 193–230 (1978).
12. Walsh-Kennedy, S. et al. Source to sink: the development of the latest Messinian to Pliocene–Quaternary Cilicia and Adana Basins and their linkages with the onland Mut Basin, eastern Mediterranean. *Tectonophysics* **622**, 1–21 (2014).
13. Akbaş, B. et al. *Geological Map of Turkey at a Scale of 1:1,250,000* (General Directorate of Mineral Research and Exploration, 2011).
14. Emre, Ö. et al. *Annotated Active Fault Map of Turkey* Special Publication Series 30 (General Directorate of Mineral Research and Exploration, 2013).
15. Reitman, N. G. et al. Offset channels may not accurately record strike-slip fault displacement: evidence from landscape evolution models. *J. Geophys. Res. Solid Earth* **124**, 13427–13451 (2019).
16. Ghoneim, E., Benedetti, M. & El-Baz, F. An integrated remote sensing and GIS analysis of the Kufrah Palaeoriver, Eastern Sahara. *Geomorphology* **139–140**, 242–257 (2012).
17. Walker, R. & Jackson, J. Offset and evolution of the Gowk fault, S.E. Iran: a major intra-continental strike-slip system. *J. Struct. Geol.* **24**, 1677–1698 (2002).
18. Hubert-Ferrari, A. et al. in *Collision and Collapse at the Africa-Arabia-Eurasia Subduction Zone* (eds Van Hinsbergen, D. J. J. et al.) 133–154 (The Geological Society of London, 2009); https://doi.org/10.1144/sp311.5
19. Westaway, R., Demir, T. & Seyrek, A. Geometry of the Turkey-Arabia and Africa-Arabia plate boundaries in the latest Miocene to Mid-Pliocene: the role of the Malatya-Ovacık Fault Zone in eastern Turkey. *eEarth Discuss.* **2**, 169–190 (2007).
20. Westaway, R. Kinematic consistency between the Dead Sea Fault Zone and the Neogene and Quaternary left-lateral faulting in SE Turkey. *Tectonophysics* **391**, 203–237 (2004).
21. McNab, R., Ball, P. W., Hoggard, M. J. & White, N. J. Neogene uplift and magmatism of Anatolia: insights from drainage analysis and basaltic geochemistry. *Geochem. Geophys. Geosyst.* **19**, 175–213 (2018).
22. Hubert-Ferrari, A., Armijo, R., King, G., Meyer, B. & Barka, A. Morphology, displacement and slip rates along the North Anatolia Fault, Turkey. *J. Geophys. Res.* **107**, ETG 9-1–ETG 9-33 (2002).
23. McClusky, S. et al. Global positioning system constraints on plate kinematics and dynamics in the eastern Mediterranean and Caucuses. *J. Geophys. Res.* **105**, 5695–5719 (2000).
24. Westaway, R. Kinematics of the Middle East and Eastern Mediterranean updated. *Turk. J. Earth Sci.* **12**, 5–46 (2003).
25. Bulut, F. et al. The East Anatolian Fault Zone: seismotectonic setting and spatiotemporal characteristics of seismicity based on precise earthquake locations. *J. Geophys. Res.* **117**, B07304 (2012).
26. Yazıcı, M., Zabcı, C., Natal'in, B. A., Sançar, T. & Akyüz, H. S. Palaeoseismic behaviour of strike-slip faults in slowly deforming regions: palaeoearthquakes and long-term slip history of the Ovacık Fault (eastern Turkey). *J. Seismol.* **25**, 255–272 (2021).
27. Meijers, M. J. M. et al. Rapid Late Miocene surface uplift of the Central Anatolian Plateau margin. *Earth Planet. Sci. Lett.* **497**, 29–41 (2018).
28. Memiş, C. et al. Long wavelength progressive plateau uplift in eastern Anatolia since 20 Ma: implications for the role of slab peel-back and break-off. *Geochem. Geophys. Geosyst.* **21**, e2019GC008726 (2020).
29. Toprak, S. & Erik, N. Y. Petrographical properties and unusual features of Kangal coals, Sivas–Turkey. *Int. J. Coal Geol.* **86**, 297–305 (2011).
30. Nazik, A. et al. Fresh and brackish water ostracods of upper Miocene deposits, Arguvan/Malatya (Eastern Anatolia). *Turk. J. Earth Sci.* **17**, 481–495 (2008).
31. Stow, D. et al. The Pliocene-Recent Euphrates river system: sediment facies and architecture as an analogue for subsurface reservoirs. *Energy Geosci.* **1**, 174–193 (2020).
32. Hussain, E., Kalaycıoğlu, S., Milliner, C. W. D. & Çakir, Z. Preconditioning the 2023 Kahramanmaraş (Türkiye) earthquake disaster. *Nat. Rev. Earth Environ.* **4**, 287–289 (2023).
33. Syvitski, J. P. M. & Milliman, J. D. Geology, geography, and humans battle for dominance over the delivery of fluvial sediment to the coastal ocean. *J. Geol.* **115**, 1–19 (2007).
34. Castelltort, S. et al. *The Source-to-Sink Vade-mecum* SEPM Concepts in Sedimentology and Paleontology Vol. 16 (SEPM, 2023); https://doi.org/10.2110/sepmcsp.16
35. Sassolas-Serrayet, T., Cattin, R. & Ferry, M. The shape of watersheds. *Nat. Commun.* **9**, 3791 (2018).
36. Bertoni, C. et al. *The Demise of a Salt Giant: Climatic-Environmental Transition during the Terminal Messinian Salinity Crisis* (International Ocean Discovery Program, 2018); https://docs.iodp.org/Proposal_Cover_Sheets/857C-Full_Bertoni_cover.pdf
37. Leroux, E. et al. High resolution evolution of terrigenous sediment yields in the Provence Basin during the last 6 Ma: relation with climate and tectonics. *Basin Res.* **29**, 305–339 (2017).
38. Meijers, M. J. M., Brocard, G. Y., Whitney, D. L. & Mulch, A. Palaeoenvironmental conditions and drainage evolution of the central Anatolian lake system (Turkey) during Late Miocene to Pliocene surface uplift. *Geosphere* **16**, 490–509 (2020).
39. Schneck, R., Micheels, A. & Mosbrugger, V. Climate modelling sensitivity experiments for the Messinian salinity crisis. *Palaeogeogr. Palaeoclimatol. Palaeoecol.* **286**, 149–163 (2010).
40. Gladstone, R., Flecker, R., Valdes, P., Lunt, D. & Markwick, P. The Mediterranean hydrologic budget from a Late Miocene global climate simulation. *Palaeogeogr. Palaeoclimatol. Palaeoecol.* **251**, 254–267 (2007).
41. Gvirtzman, Z. et al. Limited Mediterranean sea-level drop during the Messinian salinity crisis inferred from the buried Nile canyon. *Commun. Earth Environ.* **3**, 216 (2022).

42. Loncke, L., Gaullier, V., Mascle, J., Vendeville, B. & Camera, L. The Nile deep-sea fan: an example of interacting sedimentation, salt tectonics and inherited subsalt palaeotopographic features. *Mar. Pet. Geol.* **23**, 297–315 (2006).
43. Andreetto, F. et al. Freshening of the Mediterranean Salt Giant: controversies and certainties around the terminal (Upper Gypsum and Lago-Mare) phases of the Messinian salinity crisis. *Earth Sci. Rev.* **216**, 103577 (2021).
44. Ilgar, A., Nemec, W., Hakyemez, A. & Karakuş, E. Messinian forced regressions in the Adana Basin: a near-coincidence of tectonic and eustatic forcing. *Turk. J. Earth Sci.* **22**, 864–889 (2013).
45. Kürüm, S., Önal, A., Boztuğ, D., Spell, T. & Arslan, M. $^{40}Ar/^{39}Ar$ age and geochemistry of the post-collisional Miocene Yamadağ volcanics in the Arapkir area (Malatya Province), eastern Anatolia, Turkey. *J. Asian Earth Sci.* **33**, 229–251 (2008).
46. Di Giuseppe, P. et al. From subduction to strike slip-related volcanism: insights from Sr, Nd and Pb isotopes and geochronology of lavas from Sivas–Malatya region, Central Eastern Anatolia. *Int. J. Earth Sci.* **110**, 849–874 (2021).
47. Duggen, S., Hoernle, K., van den Bogaard, P., Rüpke, L. & Morgan, J. P. Deep roots of the Messinian salinity crisis. *Nature* **422**, 602–606 (2003).
48. Simon, D. & Meijer, P. Dimensions of the Atlantic–Mediterranean connection that caused the Messinian salinity crisis. *Mar. Geol.* **364**, 53–64 (2015).
49. Aloisi, G. et al. Chlorine isotopes constrain a major drawdown of the Mediterranean Sea during the Messinian salinity crisis. *Nat. Commun.* **15**, 9671 (2024).
50. Roveri, M. et al. Dense shelf water cascading and Messinian canyons: a new scenario for the Mediterranean salinity crisis. *Am. J. Sci.* **314**, 751–784 (2014).
51. Manzi, V. et al. The onset of the Messinian salinity crisis in the deep Eastern Mediterranean Basin. *Terra Nova* **30**, 189–198 (2018).
52. Taylor, C., Robinson, T. R., Dunning, S., Carr, J. R. & Westoby, M. Glacial lake outburst floods threaten millions globally. *Nat. Commun.* **14**, 487 (2023).
53. Coleman, N. M. Hydrographs of a Martian flood from a breached crater lake, with insights about flow calculations, channel erosion rates, and chasma growth. *J. Geophys. Res. Planets* **118**, 263–277 (2013).
54. Bowman, S. A. A comprehensive review of the MSC facies and their origins in the offshore Sirt Basin, Libya. *Pet. Geosci.* **18**, 457–469 (2012).
55. Griffin, D. L. The late Neogene Sahabi rivers of the Sahara and their climatic and environmental implications for the Chad Basin. *J. Geol. Soc. London* **163**, 905–921 (2006).
56. Krijgsman, W., Hilgen, F. J., Raffi, I., Sierro, F. J. & Wilson, D. S. Chronology, causes and progression of the Messinian salinity crisis. *Nature* **400**, 652–655 (1999).
57. Madof, A. S. et al. Time-probabilistic approach to the Late Miocene Messinian salinity crisis: implications for a disconnected Paratethys. *Terra Nova* **34**, 395–406 (2022).
58. Garcia-Castellanos, D. et al. Catastrophic flood of the Mediterranean after the Messinian salinity crisis. *Nature* **462**, 778–781 (2009).
59. He, C. et al. Drainage divide migration and implications for climate and biodiversity. *Nat. Rev. Earth Environ.* **5**, 177–192 (2024).
60. Afanasiyeva, N. et al. *Geological Map of Syria with an Explanatory Text* (Ministry of Petroleum and Mineral Resources, 1986).
61. Çiftçí, S. Y., Hacıköylü, P., Kalanyuva, Y. G., Kansu, E. & Tpao, A. A. Exploration plays in the Mersin Basin, Turkish Mediterranean Sea. *Leading Edge* **31**, 832–845 (2012).
62. Darbaş, G. & Nazik, A. Micropalaeontology and palaeoecology of the Neogene sediments in the Adana Basin (South of Turkey). *J. Asian Earth Sci.* **39**, 136–147 (2010).
63. Cipollari, P. et al. in *Geological Development of Anatolia and the Easternmost Mediterranean Region* (eds Robertson, A. H. F. et al.) 473–494 (The Geological Society of London, 2012); https://doi.org/10.1144/sp372.5
64. Sıncaı, M. Fluctuations of sea water temperature based on nannofloral changes during the Middle to Late Miocene, Adana Basin, Turkey. *Turk. J. Earth Sci.* **22**, 247–263 (2013).
65. Burton-Ferguson, R., Aksu, A. E., Calon, T. J. & Hall, J. Seismic stratigraphy and structural evolution of the Adana Basin, eastern Mediterranean. *Mar. Geol.* **221**, 189–222 (2005).
66. Büyükmeriç, Y. et al. Early Pliocene molluscs from the easternmost Mediterranean region (SE Turkey): biostratigraphic, ecostratigraphic and palaeobiogeographic implications. *Turk. J. Earth Sci.* **27**, 127–151 (2018).
67. Hardenberg, M. F. & Robertson, A. H. F. Sedimentology of the NW margin of the Arabian plate and the SW–NE trending Nahr El-Kabir half-graben in northern Syria during the latest Cretaceous and Cenozoic. *Sediment. Geol.* **201**, 231–266 (2007).
68. Bowman, S. A. Regional seismic interpretation of the hydrocarbon prospectivity of offshore Syria. *GeoArabia* **16**, 95–124 (2011).
69. Milliman, J. D. & Farnsworth, K. L. *River Discharge to the Coastal Ocean: A Global Synthesis* (Cambridge Univ. Press, 2013); https://doi.org/10.1017/CBO9780511781247

Publisher's note Springer Nature remains neutral with regard to jurisdictional claims in published maps and institutional affiliations.

Open Access This article is licensed under a Creative Commons Attribution 4.0 International License, which permits use, sharing, adaptation, distribution and reproduction in any medium or format, as long as you give appropriate credit to the original author(s) and the source, provide a link to the Creative Commons licence, and indicate if changes were made. The images or other third party material in this article are included in the article's Creative Commons licence, unless indicated otherwise in a credit line to the material. If material is not included in the article's Creative Commons licence and your intended use is not permitted by statutory regulation or exceeds the permitted use, you will need to obtain permission directly from the copyright holder. To view a copy of this licence, visit http://creativecommons.org/licenses/by/4.0/.

© Chevron International Exploration and Production Company Limited, Chevron U.S.A. Inc., acting through its Chevron Technical Center division and Abdallah S. Zaki, Elise J. Laugier, Claudia Bertoni, Richard T. Walker 2026

Methods

Seismic interpretation

The entirety of the Nahr Menashe was mapped in SLB's Petrel software using conventional seismic stratigraphic methods[70,71] on 2D and 3D seismic-reflection data in two-way travel time. The dataset consisted of 192 2D lines and five 3D volumes from offshore Syria, Lebanon, Israel, Cyprus and Egypt (Extended Data Fig. 1). To facilitate reflection picking, all data were phase-rotated to ensure consistent zero-phase polarity. Horizons marking the top and base of the Nahr Menashe were picked on peak reflections and were interpreted using both the Manual interpretation and Seeded 3D autotracking tools. The result was an internally consistent loop-tied framework (2D data) that intersected continuous horizons (3D data). The composite top and base horizons were then interpolated to create continuous surfaces, which were used to generate a thickness map with the Make Thickness Map tool.

Geologic mapping

Maps of the study area (Fig. 1a–e) were created by overlaying images of Late Miocene to Early Pliocene deposits[6,7,12] from the Geological Map of Türkiye[13] and Syria[60], as well as faults from the Active Fault Map of Türkiye[14], onto digital elevation models (DEMs) of the topography[72]. As part of our initial quality control measure, polygons representing Late Neogene deposits were checked against local studies to confirm their ages, lateral extents, and lithologies. Fault data were then compared to local and regional studies to verify their lengths and orientations. Where necessary, adjustments were made to reflect convergent interpretations. After validating the spatial and temporal positions of deposits and faults, DEMs were selected from the United States Geological Survey (USGS) EarthExplorer (https://www.usgs.gov/tools/earthexplorer, accessed 10 November 2022) covering parts of Türkiye, Syria and Iraq. The 84 tiles (1° latitude by 1° longitude) from the Shuttle Radar Topography Mission (SRTM) were downloaded from the USGS Earth Resources Observation and Science (EROS) Center Archive (https://doi.org/10.5066/F7PR7TFT). Each tile had a lateral resolution of a 1 arc-second (~30 m) and a vertical resolution of <16 m. Tiles were converted to the georeferenced Tagged Image File Format (geoTIFF) and merged using the Mosaic to New Raster tool in ArcMap 10.8.1. A multidirectional hillshade image was generated from the mosaiced DEM using the Hillshade Raster Function within ArcGIS Pro 3.0.2 and saved as a jpeg (Joint Photographic Experts Group). Geologic maps were georeferenced by applying a third-order polynomial transformation using at least ten control points, done with the Georeference tool in ArcGIS Pro 3.0.2. The final georeferenced geologic maps (TIFF format) were superimposed over DEMs (jpeg format) in Adobe Illustrator, where accumulations and faults were digitized.

For calculating the geologic age of mapped palaeo-pathways offset by strike–slip faults, channel offset lengths were measured and long-term slip rates were compiled from previous studies. To account for uncertainty in the channel offset lengths[15], minimum, maximum and preferred measurements were recorded for each fault (using the path function in Google Earth Pro). Mean offset lengths were then calculated, noting that the preferred values—and thus the means—were not consistently centred between the minimum and maximum measurements. Similarly, uncertainties in long-term slip rates were calculated by averaging values from earlier studies, such as those associated with the EAF[20,22–25], NAF[18,22] and Ovacık Fault[26]. To determine geologic age, average channel offset lengths were divided by average long-term slip rates; these values were then used to restore palaeo-pathways to their mean pre-offset orientations (Fig. 1f–j).

Profile extraction

The paths of the Palaeo-Karasu and Palaeo-Murat rivers (Fig. 2a–c) were traced in Google Earth Pro (using the path function) by manually identifying continuous active or abandoned channels, giving particular attention to those overlying Late Miocene to Early Pliocene riverine deposits. Coastal profiles (Fig. 2d,e), however, were chosen using the locations of pre-existing surface and subsurface data, such as outcrop, well log, core and seismic data[61–68]. Completed paths were exported as KML files and loaded into ArcGIS Pro 3.0.2, where they were converted to polylines using the KML To Layer tool. To generate profiles, the Points Along Line tool was used to resample the paths to equally spaced points (500 m), and these points were extracted from the merged DEM using the Extract Values to Points tool. Lateral (x and y) and vertical (elevation) values were exported for plotting; these data were then processed and plotted in Microsoft Excel, and the final profiles were digitized in Adobe Illustrator.

BQART modelling

We modelled the Palaeo-Karasu and Palaeo-Murat basins using the following empirical equations[33]:

$$Q_s = \omega B Q_w^{0.31} A^{0.5} R T$$

$$B = I L (1 - T_E) E_h$$

$$I = 1 + 0.09 A_g$$

where Q_s is the sediment discharge (MT yr^{-1}), ω is a constant (0.0006), B is related to geologic and anthropogenic factors, Q_w is water discharge (km^3 yr^{-1}), A is basin area (km^2), R is relief (km), T is temperature (°C), I is a glacier erosion factor (unitless and dimensionless; $I \geq 1$), L is an average lithology factor (unitless and dimensionless), T_E is the trapping efficiency of lakes and human-made reservoirs (unitless and dimensionless; $1 - T_E \leq 1$), E_h is the human-influenced soil-erosion factor (unitless and dimensionless), and A_g is the percentage of the catchment area that was glaciated.

For the Palaeo-Karasu River, we calculated Q_s by first determining the volume of the Handere using a contour map from ref. 12 (their fig. 9). We imported this map as a TIFF into Petrel, digitized the contours as polygons, and converted them to a surface using the Make Surface tool (Fig. 3c). The Volume Below Surface tool yielded a total volume of 8,313 km^3. Using a sediment density of 2,000 MT km^{-3} (2,000 kg m^{-3}), we converted volume to mass and divided by the interpreted deposit duration (120 kyr; ref. 6), yielding a Q_s of 139.2 MT yr^{-1}. For the Palaeo-Murat, we derived Q_s by using the Nahr Menashe isochron (in seconds) and then converted it to thickness (in metres) using a sediment velocity of 2,925 m s^{-1} (Fig. 3d)[7]. The Volume Below Surface tool yielded a total volume of 3,372 km^3. Using the same density and duration as for the Handere, we obtained a Q_s of 56.2 MT yr^{-1}.

After calculating Q_s, we used three steps to approximate the input parameters for the Palaeo-Karasu and Palaeo-Murat basins (Extended Data Table 1a,b). First, we made an initial approximation of A using the lateral extent of Late Miocene to Early Pliocene accumulations and the position of faults, and we ensured that the estimates respected the upper bound of available space in Anatolia and the lower bound of the surface areas of the Handere and Nahr Menashe. We then estimated the initial ranges of Q_w by multiplying these values of A by annual palaeo-precipitation estimates (200–1,000 mm)[73,74]. Second, we generated an iterative set of BQART models using the A and Q_w from the first step, together with R and T values from published studies[21,39]. We then compared the resulting Q_s values to the estimated Q_s and adjusted A—and thus Q_w—until the deterministic Q_s matched the estimated value. Lastly, we ran two probabilistic BQART models (N = 250,000 realizations for each of the Palaeo-Karasu and Palaeo-Murat basins) using Crystal Ball[72], which draws input values from user-defined distributions to probabilistically model the outcome of deterministic equations. We selected realizations that resulted in Q_s within 15% of those calculated for the Palaeo-Karasu and Palaeo-Murat rivers (Fig. 3a), resulting in 146,465 and 109,393 runs, respectively. As a validation step,

we checked modelled values of A against those calculated from the following empirical equation (modified Hack's Law)[35]:

$$A = \frac{L}{S^{-0.6}}$$

where A is basin area (km^2), L is river length (km) and S is catchment shape (unitless and dimensionless; 1 is circular and 2.5 is elongate). We output final values using Microsoft Excel and digitized the graphs with Adobe Illustrator. To delineate the catchments of the Palaeo-Karasu and Palaeo-Murat basins, we constrained the P50 values of A by fault positions and the occurrence of Late Miocene to Early Pliocene accumulations (Fig. 3b). Additionally, for model runs versus sediment discharge, we plotted water discharge, basin area, maximum relief, and temperature as histograms (and also tornado diagrams) in MATLAB, with the final images digitized using Adobe Illustrator (Extended Data Figs. 2a–f and 3a–f). We used a similar procedure to create plots of sediment discharge versus basin area (Fig. 3e) and water discharge (Fig. 3f).

To quantify the surface area percentage of the exposed lithology constrained by the P50 catchments of the Palaeo-Karasu and Palaeo-Murat basins, we imported shapefiles from the Geological Map of Türkiye[13] into ArcGIS Pro 3.0.2. For comparison to the Handere, we concatenated and filtered polygons according to the classification of ref. 6 (their table 1); we summed surface areas from polygons for each rock type and clipped to the P50 basin area using Clip Analysis from the Analysis Toolbox. We then imported the data and plotted them in Microsoft Excel (Fig. 3c,d), with the final pie charts digitized in Adobe Illustrator.

Landscape reconstruction

We reconstructed the eastern Mediterranean during the latest Messinian using palaeo-elevation, facies belts and depositional textures as primary inputs (Fig. 4). Palaeo-elevation shapefiles (ranging from −2,000 m to +1,500 m) were created from contour maps (ref. 21, their fig. 6l,m; ref. 41, their fig. 2f), which we imported into Google Earth Pro, georeferenced, digitized as paths and edited, and exported as KML files. We imported these final KML files into ArcGIS Pro 3.0.2 and converted them to polylines using the KML To Layer tool. Although we modified several facies belts from pre-existing interpretations[6,7,12,13,42,75–78], we generated most of them using a rule-based criterion that linked depositional environment, Messinian evaporite thickness[10] and the gradient of the modern seafloor (Extended Data Table 2). After establishing this criterion, we applied the same methodology (above) to create facies-belt shapefiles in ArcGIS Pro 3.0.2. Photographic analogues from modern dryland fluvio-lacustrine environments in Australia, Iran, Israel, Kazakhstan, New Zealand, Pakistan, Russia, Türkiye and the United States were retrieved using Google Earth Pro, and their locations were saved as placemarks.

Using palaeo-elevation and facies-belt shapefiles, together with depositional textures, we employed a three-step process to reconstruct the eastern Mediterranean in 3D. First, we created a surface in Global Mapper using shapefiles. Where palaeo-isolines were missing or sparse, we used vertical warping of the modern topography-bathymetry to create a continuous surface. We then utilized Houdini and Blender to warp, re-map, sculpt and blend the restored surface. Second, we draped depositional textures—gathered from Google Earth—onto the restored surface, completing the texturing in Houdini, World Machine and Substance Painter using facies-belt shapefiles and texture masks (PNG (portable network graphic) files). Finally, we adjusted, rendered and applied final image enhancements to the reconstructed surface in Blender and Affinity, and used Adobe Illustrator to mark physiographic features on the final PNG.

Limitations and uncertainties

Although the study presented here introduces a hypothesis for the origin of the ancestral Euphrates River, several limitations and uncertainties remain. These include the absence of field-based data, the reliance on modern topography to reconstruct ancient riverine courses, the use of fault offset lengths and long-term slip rates to invert for palaeo-pathway age, and the application of the BQART model to infer sediment discharge. Addressing these constraints—and rigorously testing the proposed existence of the Palaeo-Karasu and Palaeo-Murat rivers, and their relationship to the modern Euphrates River—will require future work that integrates stratigraphic, geomorphic and geochronologic data, supported by targeted sensitivity analyses.

Whereas our geologic–geomorphic reconstructions and BQART modelling support the presence of large fluvial systems terminating in a partially desiccated eastern Mediterranean, our hypothesis may be further tested using field-based data, such as those related to fluvio-lacustrine deposits and palaeo-current indicators. Correlating fluvio-lacustrine accumulations throughout the study area could help reconstruct ancient depositional environments, avulsion histories and patterns of sediment dispersal, while measurements of palaeo-current indicators may constrain flow orientations, channel-migration patterns and source-to-sink dynamics. Taken together, these measurements could be used to interpret climatic changes and tectonic reorganization of drainage networks, particularly those related to Anatolian uplift and the MSC. However, given the extensive length of the reconstructed pathways, their high sinuosity, and the discontinuous nature of surface exposure, obtaining correlated fluvio-lacustrine sections and statistically robust palaeo-current data across such terrain presents major logistical and methodological challenges.

In addition to surficial (field-based) data, subsurface datasets can help reconstruct palaeo-pathways. Regional studies that have integrated onshore topographic maps with offshore seismic data have shown that the Messinian-aged Palaeo-Nile River[79] supplied the Abu Madi incised valley fill[75] (offshore Egypt), whereas the Palaeo-Kufrah River[55] sourced the Eosahabi fluvial fan[54] (offshore Libya). Our reconstruction of the Palaeo-Karasu and Palaeo-Murat river systems—based on topographic mapping and seismic interpretation—follows a similar methodological approach and similarly identifies fluvial networks supplying sediment to the Handere and Nahr Menashe. Although the specific details of these palaeo-pathways remain tentative, our mapping offers a first-order approximation. More importantly, our integrated topographic-seismic framework extends the analysis into the Euphrates River headwaters, providing evidence that fluvial systems delivered sediment directly into a partially desiccated eastern Mediterranean during the terminal MSC.

Whereas seismic and topographic data have been successfully used to trace ancient fluvial systems in tectonically quiescent regions, extending such reconstructions into tectonically active settings introduces additional uncertainties. As such, establishing a chronological framework in these environments often relies on reconstructing displacement histories from fault offset lengths and long-term slip rates—an approach widely used in tectonic and seismic hazard studies[80,81]. Although the duration of these reconstructions (tens to hundreds of thousands of years) are substantially shorter than those calculated for the Palaeo-Karasu and Palaeo-Murat rivers, studies along the NAF demonstrate that long-term slip rates can be constrained over timescales of at least 13 Ma (ref. 82), based on cumulative displacement and sediment dating. However, although this extension underscores the method's potential for long-term reconstructions, it also highlights its inherent limitations, particularly its tendency to oversimplify the spatio-temporal variability of fault motion. This simplification becomes especially problematic when attempting to reconstruct fluvial pathways across regions characterized by distributed deformation and episodic rupture. These challenges are amplified in our study area, where palaeo-seismic and geomorphic slip-rate estimates are sparse and GPS/InSAR (Global Positioning System/interferometric synthetic aperture radar) coverage remains limited, resulting in reconstructions that represent a pragmatic compromise between data availability and

tectonic complexity. Further complicating matters, rivers in tectonically active landscapes are prone to dynamic reorganization—including capture[83]—which obscures evidence of stable, long-term pathways. Our reconstructions therefore assume a degree of fluvial stability that may not be applicable over a 10-Myr timescale, particularly in regions prone to drainage capture and reorganization. However, our interpretations are constrained by preserved geomorphic and stratigraphic features, which we interpret as indicators of sustained fluvial flow and sediment delivery.

Although the BQART model provides a practical framework for estimating sediment discharge based on empirical relationships, its application to ancient fluvial systems introduces several uncertainties. First, the model assumes a relatively stable hydrologic regime over the duration of deposition, which may not hold for the Late Miocene MSC, a period characterized by tectonic uplift, climatic variability and possible mega-flood events. Second, the estimated accumulation duration (120 kyr for both the Handere and Nahr Menashe) is constrained by biostratigraphy and geochronology, but it may not capture the full temporal range. Third, the inversion of BQART involves interdependent variables—basin area (A), water discharge (Q_w) and sediment discharge (Q_s)—which introduces nonlinearities that can propagate uncertainty across model outputs. Although our probabilistic approach mitigates some of these effects by exploring wide input ranges, the stability of inverted basin areas remains contingent on these coupled relationships. Finally, although our study focuses on BQART-based inversion, we recognize that predictive models (forward stratigraphic or landscape evolution approaches) offer dynamic perspectives on sediment routing and catchment evolution. Future work integrating these approaches, alongside improved palaeo-hydrologic proxies and climate simulations, could refine source-to-sink reconstructions under complex tectonic conditions.

Data availability

Data supporting the geologic–geomorphic maps (Fig. 1) and the BQART modelling results (Fig. 3, Extended Data Figs. 2 and 3 and Extended Data Table 1) are publicly available via figshare at https://doi.org/10.6084/m9.figshare.31382929 (ref. 72). Beyond these publicly archived materials, the study incorporates subsurface interpretations based on proprietary offshore seismic datasets from Syria, Lebanon, Israel, Cyprus and Egypt (Extended Data Fig. 1). Syrian 2D seismic data acquired by CGGVeritas (now Viridien) were used; however, their current commercial availability is uncertain and may require direct inquiry through the Viridien GeoStore (https://earthlibrary-geostore.viridiengroup.com/). Seismic datasets from Lebanon, Cyprus and Egypt (2D and 3D) were obtained from the TGS Eastern Mediterranean multiclient library (https://map.tgs.com/myTGSMap/Data-Library#33.354887,34.052551,7z). Israeli 2D seismic data may be requested through the Israel Ministry of Energy (https://prime.energy.gov.il/gismap). All proprietary datasets must be obtained directly from the respective providers, as they cannot be shared by the authors.

Code availability

Custom code was not developed for this study. Instead, probabilistic BQART analysis (adapted directly from ref. 33) was performed using the commercial software Oracle Crystal Ball (https://www.oracle.com/applications/crystalball/).

References

70. Brown, A. R. in *AAPG Memoir 42 and SEG Investigations in Geophysics No. 9: Interpretation of Three-Dimensional Seismic Data* (eds Laubach, S. E. & Grechka, V.) 103–156 (American Association of Petroleum Geologists and the Society of Exploration Geophysicists, 2011); https://doi.org/10.1190/1.9781560802884.chp4
71. Posamentier, H. W., Paumard, V. & Lang, S. C. Principles of seismic stratigraphy and seismic geomorphology I: extracting geologic insights from seismic data. *Earth Sci. Rev.* **228**, 103963 (2022).
72. Madof, A. S. NGS-2025-03-00991. *figshare* https://doi.org/10.6084/m9.figshare.31382929 (2026).
73. Blanc, P.-L. Improved modelling of the Messinian salinity crisis and conceptual implications. *Palaeogeogr. Palaeoclimatol. Palaeoecol.* **238**, 349–372 (2006).
74. Fauquette, S. et al. How much did climate force the Messinian salinity crisis? Quantified climatic conditions from pollen records in the Mediterranean region. *Palaeogeogr. Palaeoclimatol. Palaeoecol.* **238**, 281–301 (2006).
75. Abdel Aal, A. et al. Tectonic evolution of the Eastern Mediterranean Basin and its significance for hydrocarbon prospectivity in the ultradeep water of the Nile Delta. *Leading Edge* **19**, 1086–1102 (2000).
76. Moneron, J. & Gvirtzman, Z. Late Messinian submarine channel systems in the Levant Basin: challenging the desiccation scenario. *Geology* **50**, 1366–1371 (2022).
77. Lofi, J. *Seismic Atlas of the Messinian Salinity Crisis Markers in the Mediterranean Sea—Volume 2* (Commission for the Geological Map of the World and the French Geological Society, 2018); https://ccgm.org/en/product/seismic-atlas-of-the-messinian-salinity-crisis-markers-in-the-mediterranean-sea-vol-2/
78. Krijgsman, W. et al. The Gibraltar Corridor: watergate of the Messinian salinity crisis. *Mar. Geol.* **403**, 238–246 (2018).
79. Barber, P. M. Messinian subaerial erosion of the Proto-Nile delta. *Mar. Geol.* **44**, 253–272 (1981).
80. Lindvall, S. C. & Rockwell, T. K. Holocene activity of the Rose Canyon fault zone in San Diego, California. *J. Geophys. Res.* **100**, 24,121–24,132 (1995).
81. Spotila, J. A. & Anderson, K. B. Fault interaction at the junction of the Transverse Ranges and Eastern California shear zone: a case study of intersecting faults. *Tectonophysics* **379**, 43–60 (2004).
82. Hubert-Ferrari, A., Armijo, R., King, G. & Meyer, B. Morphology, displacement, and slip rates along the North Anatolian Fault, Turkey. *J. Geophys. Res.* **107**, ETG 9-1–ETG 9-33 (2002).
83. Willett, S. D., McCoy, S. W., Perron, J. T., Goren, L. & Chen, C.-Y. Dynamic reorganization of river basins. *Science* **343**, 1248765 (2014).

Acknowledgements

A.S.M. thanks Chevron, J. M. Francis and A. Paez for allowing publication, A. D. Harris and J. A. Parker for thoughtful comments regarding the manuscript, and TGS for the use of seismic data. C.B. and R.W. acknowledge partial funding from the Leverhulme Trust Research Project Grant 'NEPTUNE' (RPG-2018-243).

Author contributions

A.S.M. conceived the idea, constructed the figures, wrote the manuscript (with input from F.J.L., S.E.B. and A.S.Z.), compiled the data, mapped the geology, identified the riverine paths, gathered the literature, and assisted in creating the palaeogeographic reconstruction. F.J.L. discussed the idea, downloaded the DEMs, and plotted the elevations. S.E.B. discussed the idea, ran the BQART models, edited the manuscript, and assisted in tracing the riverine paths. A.S.Z. discussed the idea and supported creating the figures. E.J.L. merged and normalized the DEMs. C.B. and R.T.W. discussed the idea and supported creating the figures. C.R. discussed the idea and assisted with calculating ages.

S.C.L. discussed the idea and assisted with identifying depositional analogues. All authors reviewed the manuscript, examined the figures and verified the analyses.

Competing interests
The authors declare no competing interests.

Additional information
Extended data is available for this paper at https://doi.org/10.1038/s41561-026-01962-x.

Correspondence and requests for materials should be addressed to Andrew S. Madof.

Peer review information *Nature Geoscience* thanks Robert Bussert and Angelo Camerlenghi and the other, anonymous, reviewer(s) for their contribution to the peer review of this work. Primary Handling Editor: James Super, in collaboration with the *Nature Geoscience* team.

Reprints and permissions information is available at www.nature.com/reprints.

https://doi.org/10.1038/s41561-026-01962-x

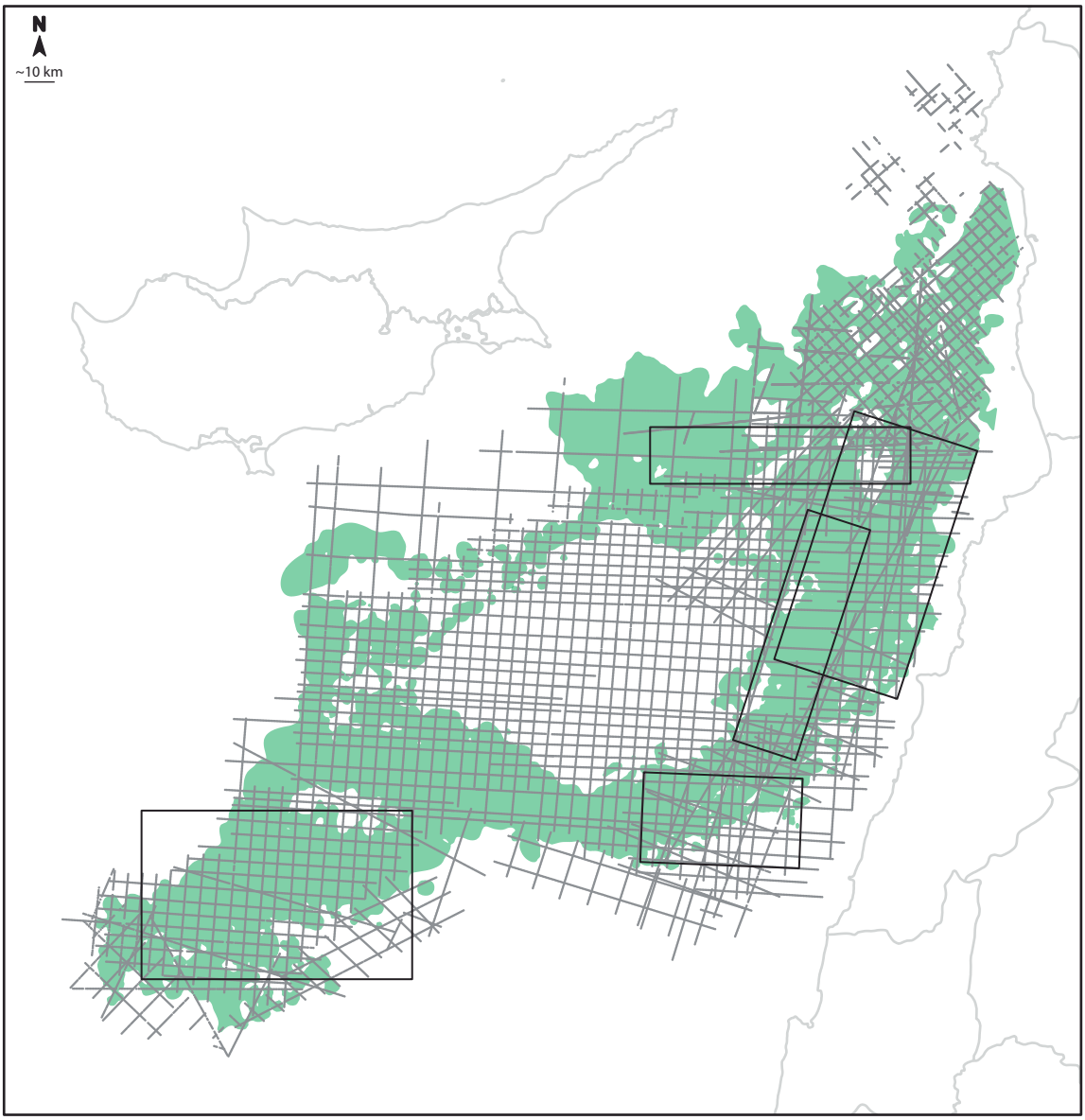

Extended Data Fig. 1 | Seismic dataset used to interpret Nahr Menashe. The dataset consists of 192 2D seismic-reflection profiles (grey lines) and five 3D volumes (black boxes) located offshore Syria, Lebanon, Israel, Cyprus, and Egypt. Green polygon shows the extent of the Nahr Menashe. Basemap created in ArcGIS Pro 3.0.2.

https://doi.org/10.1038/s41561-026-01962-x

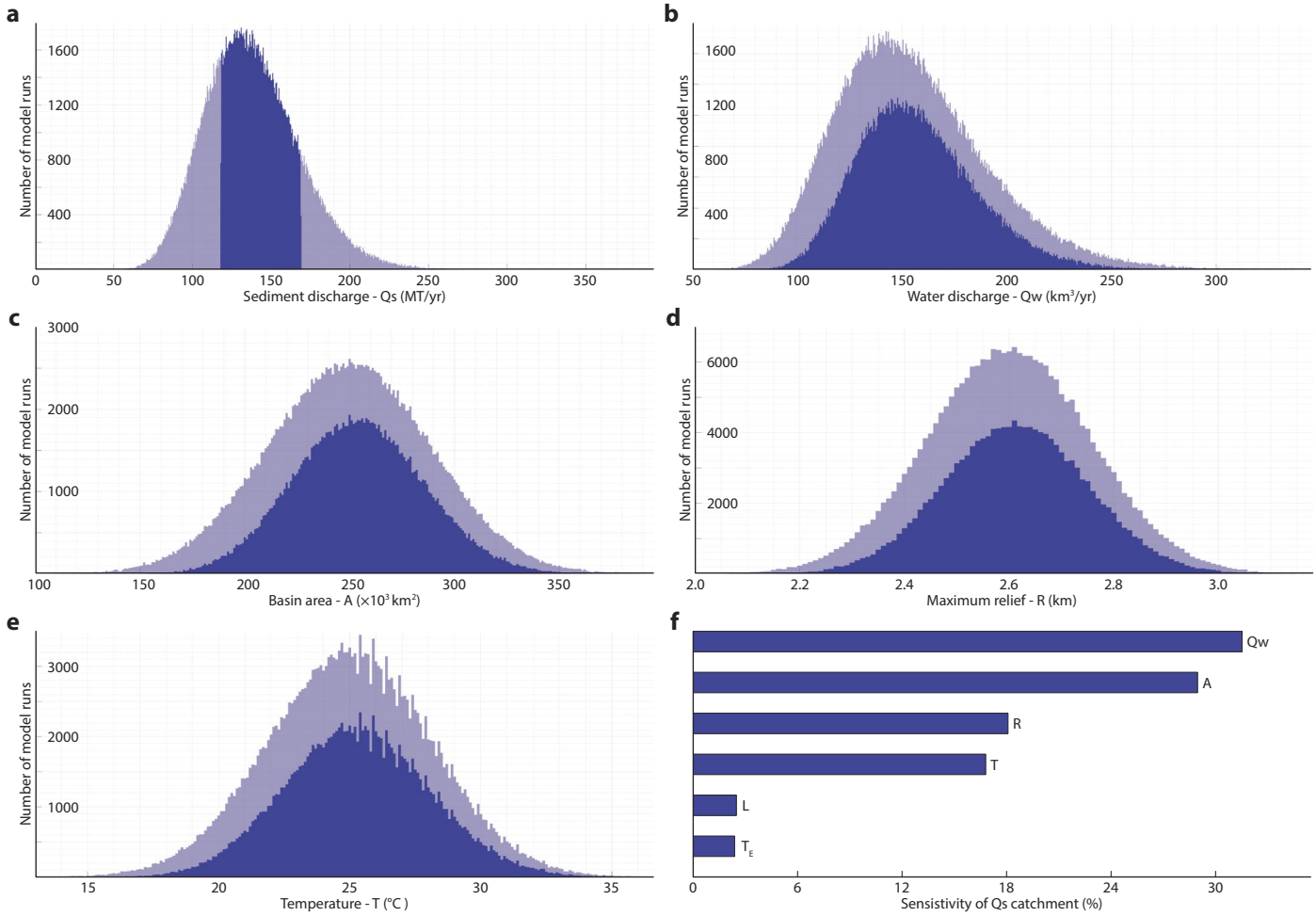

Extended Data Fig. 2 | Results of probabilistic BQART model for the Palaeo-Karasu Basin. (**a**), Sediment discharge for all model runs (250,000 runs – light blue) and those that fall within 15% of the calculated value for the Handere (139.2 MT/yr; 146,465 runs – dark blue). The latter was used to filter values for water discharge (**b**), basin area (**c**), maximum relief (**d**), and temperature (**e**). Tornado diagram (**f**) shows the sensitivity of modelled outputs to variations in inputs, with water discharge (Qw) exerting the greatest influence.

https://doi.org/10.1038/s41561-026-01962-x

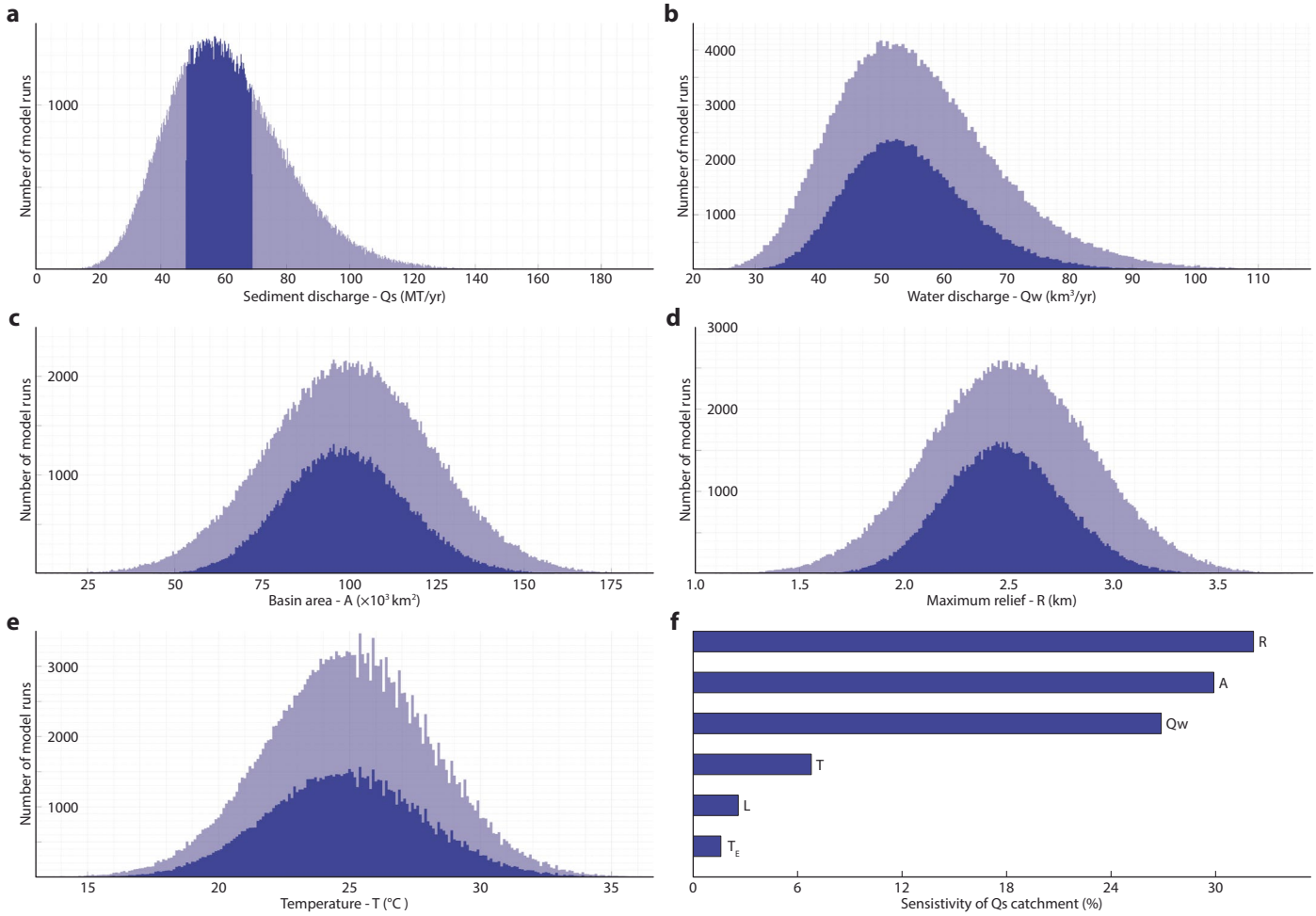

Extended Data Fig. 3 | Results of probabilistic BQART model for the Palaeo-Murat Basin. (**a**), Sediment discharge for all model runs (250,000 runs – light blue) and those that fall within 15% of the calculated value for the Nahr Menashe (56.2 MT/yr; 109,393 runs – dark blue). The latter was used to filter values for water discharge (**b**), basin area (**c**), maximum relief (**d**), and temperature (**e**). Tornado diagram (**f**) shows the sensitivity of modelled outputs to variations in inputs, with relief (R) exerting the greatest influence.

https://doi.org/10.1038/s41561-026-01962-x

Extended Data Table 1 | Input parameters for probabilistic BQART modelling

a

Catchment code	Omega	Glacial erosion factor	Lithology factor			Trapping efficiency			Anthropogenic factor
	ω(MT/yr)	I Constant	L			T_E			Eh
			Low	Mid	High	Low	Mid	High	
1	0.0006	1	1.5	1.75	2.0	0.10	0.15	0.20	1
Assumption	Constant	Constant	Triangular (min, mode, max)			Triangular (min, mode, max)			Constant

Water discharge			Basin area			Maximum relief			Temperature		
Q_w (km^3/yr)			A (km^2)			R (km)			T (°C)		
Low	Mid	High	Low	Mid	High	Low	Mid	High	Low	Mid	High
112.5	157.5	202.5	200,000	250,000	300,000	2.4	2.6	2.8	21	25	29
Log Normal (P10, P90)			Gaussian (P10, P90)			Gaussian (P10, P90)			Gaussian (P10, P90)		

b

Catchment code	Omega	Glacial erosion factor	Lithology factor			Trapping efficiency			Anthropogenic factor
	ω(MT/yr)	I Constant	L			T_E			Eh
			Low	Mid	High	Low	Mid	High	
1	0.0006	1	1.5	1.75	2.0	0.10	0.15	0.20	1
Assumption	Constant	Constant	Triangular (min, mode, max)			Triangular (min, mode, max)			Constant

Water discharge			Basin area			Maximum relief			Temperature		
Q_w (km^3/yr)			A (km^2)			R (km)			T (°C)		
Low	Mid	High	Low	Mid	High	Low	Mid	High	Low	Mid	High
40.5	56.7	72.9	70,000	90,000	130,000	2.0	2.4	3.0	21	25	29
Log Normal (P10, P90)			Gaussian (P10, P90)			Gaussian (P10, P90)			Gaussian (P10, P90)		

a, The Palaeo-Karasu Basin was modelled using the following values from the Handere: 8,313 km^3 (total volume – this study); 120 kyr (from biostratigraphy and geochronology – ref. 6); and 139.2 MT/yr (this study). b, The Palaeo-Murat Basin was modelled using the following values from the Nahr Menashe: 3,372 km^3 (total volume – this study); 120 kyr (consistent with Handere); and 56.2 MT/yr (this study). Values of lithologies, trapping efficiencies, and anthropogenic factors were taken from ref. 33; values of water discharges and basin areas were calculated from the probabilistic BQART model; values of maximum reliefs were derived from ref. 21; and values of temperatures were estimated from ref. 39.

https://doi.org/10.1038/s41561-026-01962-x

Extended Data Table 2 | Criteria used to create facies belts for reconstruction

Facies belt	Messinian thickness (m)	Relative gradient
Lacustrine (onshore)	0	-
Alluvial bypass	0	Low
Alluvial incision	0	High
Alluvial salt flats (upper)	0-500	Intermediate
Alluvial salt flats (lower)	500-1,500	Low
Lacustrine evaporitic shorelines	1,500-2,000	Low
Shallow lacustrine (offshore)	2,000-2,500	Low
Deep lacustrine (offshore)	2,500-3,000	Low

Facies belts were interpreted by linking fluvio-lacustrine depositional environments to the thickness of Messinian evaporites and associated accumulations (ref. 10), as well as the relative gradient of the modern bathymetry. Whereas the extent of onshore lakes was delineated from accumulations in ref. 13, the distribution of offshore lakes was defined primarily from Messinian thickness.